

Origin of micron-scale propagation lengths of heat-carrying acoustic excitations in amorphous silicon

Taeyong Kim,¹ Jaeyun Moon,^{2,3} and Austin J. Minnich^{1,*}

¹*Division of Engineering and Applied Science,
California Institute of Technology, Pasadena, California 91125, USA*

²*Department of Materials Science and Engineering,
University of Tennessee, Knoxville, Tennessee 37996, USA*

³*Shull Wollan Center—a Joint Institute for Neutron Sciences,
Oak Ridge National Laboratory, Oak Ridge, Tennessee 37831, USA*

(Dated: March 4, 2024)

Abstract

The heat-carrying acoustic excitations of amorphous silicon are of interest because their mean free paths may approach micron scales at room temperature. Despite extensive investigation, the origin of the weak acoustic damping in the heat-carrying frequencies remains a topic of debate. Here, we report measurements of the frequency-dependent mean free path in amorphous silicon thin films from $\sim 0.1 - 3$ THz and over temperatures from 60 - 315 K using picosecond acoustics and transient grating spectroscopy. The mean free paths are independent of temperature and exhibit a Rayleigh scattering trend from $\sim 0.3 - 3$ THz, below which the trend is characteristic of damping from density fluctuations or two-level systems. The observed trend is inconsistent with the predictions of numerical studies based on normal mode analysis but agrees with diverse measurements on other glasses. The micron-scale MFPs in amorphous Si arise from the absence of Akhiezer and two-level system damping in the sub-THz frequencies, leading to heat-carrying acoustic excitations with room-temperature damping comparable to that of other glasses at cryogenic temperatures.

* aminnich@caltech.edu

I. INTRODUCTION

The collective acoustic excitations of amorphous solids are of fundamental interest due to their anomalous properties compared to those of crystalline solids, including an excess heat capacity at cryogenic temperatures [1, 2] and damping by two-level systems [3–7]. The dispersion and damping of acoustic excitations responsible for heat transport have been extensively explored in many glasses using experimental methods such as inelastic scattering [8–13], tunnel junction spectroscopy [14], Brillouin scattering [15–17], and picosecond acoustics [18, 19], among others. These studies have generally found that excitations with well-defined frequency and wave vector are supported up to ~ 1 THz. In vitreous silica, a relative of amorphous silicon (aSi), the attenuation exhibits several different regimes, yielding different power-law frequency dependencies. For frequencies below ~ 600 GHz the damping scales as ω^{-2} corresponding to anharmonic damping and thermally activated two-level system relaxation. Between 600 GHz and 1 THz, a Rayleigh scattering trend of ω^{-4} is observed, followed by a return to ω^{-2} scaling [8]. At still higher frequencies, Kittel proposed that attenuation is independent of frequency if the wavelength is comparable to the interatomic length scale [20]. Considering these different regimes, the general trend of MFP versus frequency of acoustic excitations in glasses has been presented in Fig. 7 of Ref. [21] and Fig. 3 of Ref. [22], among others [23, 24].

Amorphous silicon is an anomalous glass for several reasons. First, at ultrasonic frequencies, attenuation by two-level systems is observed in vitreous silica but not in aSi, suggesting a low density of these systems in aSi [25, 26]. Second, thermal transport measurements indicate that the thermal conductivity of aSi can be higher than those of most glasses [27–30] and that heat-carrying acoustic excitations travel distances on the order of one micron at room temperature despite the atomic disorder [30–32]. This value is far larger than few nanometer value inferred for vitreous silica at room temperature [22, 23].

Experimentally resolving the attenuation coefficients by frequency in the sub-THz frequency band would help to understand the origin of these properties, but probing acoustic excitations in this regime is a long-standing experimental challenge. Amorphous silicon is synthesized in small volumes as a thin film of at most a few microns, precluding the use of high-resolution inelastic neutron scattering. Even if sufficient volumes were available, kinematic constraints complicate the measurement of the dispersion and broadening

of low energy excitations. While inelastic x-ray scattering has been successfully applied to study THz excitations in aSi [9], the energy resolution is not sufficient to resolve sub-THz excitations. Picosecond acoustics and Brillouin scattering are generally unable to access frequencies above ~ 100 GHz, while tunnel junction spectroscopy and cryogenic thermal conductivity measurements require films with thickness of several millimeters.

As a result, studies of the acoustic excitations in aSi have relied on numerical simulations based on normal mode analysis. Feldman and Allen classified the excitations in aSi as propagons, diffusons, and locons according to the qualities of the normal mode eigenvectors [33]. Fabian and Allen computed anharmonic decay rates of the normal modes of aSi, predicting that they should exhibit a clear temperature dependence [34]. Other molecular dynamics simulations based on normal mode analysis have predicted that the MFPs decrease as ω^{-2} with increasing frequency for excitations of a few THz frequency, leading to the conclusion that they are damped by anharmonicity [35, 36]. However, some of these predictions are not supported by experiment. For instance, the predicted temperature dependence of THz excitations in Ref. [34] is not observed experimentally using inelastic x-ray scattering [9]. In the hypersonic frequency band ~ 100 GHz, the measured values of attenuation are lower than those predicted by anharmonic damping [37].

An experimental approach to measure the damping of sub-THz phonons versus frequency and thereby resolve this discrepancy is needed. For solids like aSi with MFPs in the micron range, transient grating (TG) is a tabletop experimental method that is capable of measuring the MFP accumulation function, or the cumulative thermal conductivity distribution versus MFP [38–40]. The technique relies on observations of non-diffusive thermal transport to constrain this function; knowledge of the acoustic dispersion of the solid then provides the MFP versus frequency. In the case of amorphous silicon, the dispersion is known and isotropic [9, 41], simplifying the analysis further. Combined with picosecond acoustics and inelastic x-ray scattering for the low and high frequency limits of the attenuation coefficient, respectively, TG measurements could constrain the frequency dependence of the damping in the sub-THz frequency band and thus resolve the discrepancy.

Here, we report the measurement of the frequency-dependent MFPs of sub-THz acoustic excitations in a free-standing aSi thin film using this approach. The measured MFPs are independent of temperature and exhibit a Rayleigh-type scattering trend from $\sim 0.3 - 3$ THz, below which the trend is characteristic of damping by density fluctuations or two-

level systems. These trends are inconsistent with predictions from normal mode analysis but agree with the trends measured in other glasses. The distinguishing feature of aSi is the weak Akhiezer or two-level system damping of sub-THz vibrations, leading to acoustic attenuation in aSi at room temperature comparable to that of vitreous silica at ~ 1 K. The result is micron-scale propagation lengths of heat-carrying acoustic excitations at room temperature in aSi.

II. EXPERIMENT

We used TG to measure the thermal diffusivity of free-standing aSi thin films with variable grating period from $\sim 0.75 - 15.7 \mu\text{m}$. The sample is prepared by depositing aSi on a silicon nitride substrate using chemical vapor deposition as described in Ref. [9]. A free-standing membrane is prepared by dry-etching the handle wafer and the nitride, yielding a free-standing amorphous silicon membrane of ~ 500 nm thickness and 1 mm^2 cross-sectional area. A scanning electron microscope image of the sample is given in Fig. 1A.

The transient grating setup is identical to that described in Refs. [39, 40] and is illustrated schematically in Fig. 1A. Briefly, a pair of pump pulses (wavelength 515 nm, pulse duration ≈ 1 ns, repetition rate 200 Hz, $520 \mu\text{m } 1/e^2$ diameter) is focused on the sample to create a spatially periodic heating profile with grating period (L) and wave vector ($q = 2\pi/L$) defined by the incident angle. A continuous wave laser beam (wavelength 532 nm, chopped at 3.2% duty cycle to minimize steady heating, $470 \mu\text{m } 1/e^2$ diameter) diffracts from the grating, monitoring its thermal relaxation. We employ a heterodyne detection method to increase the signal-to-noise ratio [42]. The optical powers were chosen to yield adequate signal-to-noise ratio while minimizing steady heating (see SI Sec. III for additional discussion).

III. RESULTS

We conducted TG measurements versus grating period at several temperatures and versus temperature at a fixed grating period of $L = 10.7 \mu\text{m}$. Figure 1B shows representative signal traces at ~ 315 K (additional data and fits are provided in SI Sec. II). The decay exhibits a single exponential profile with a time constant in the range of tens of nanoseconds to microseconds due to thermal transport. The thermal diffusivity is obtained by extracting

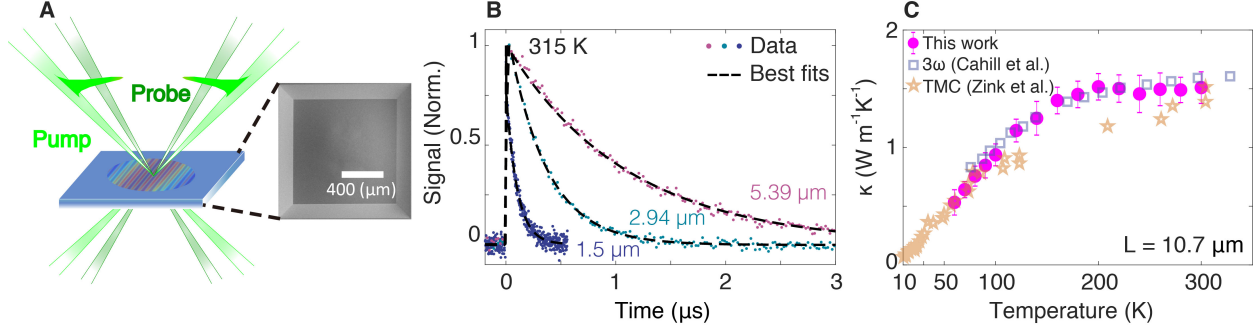


Figure 1. (A) Schematic of the TG experiment. Two pump laser pulses are interfered on the sample, impulsively creating a spatially periodic temperature rise. The probe beams diffract from the transient grating, monitoring the thermal relaxation. A scanning electron microscope image of the free-standing amorphous silicon membrane is shown. (B) Representative measured signals versus time and single exponential fits for aSi at 315 K for various grating periods. (C) Measured thermal conductivity versus temperature for $L = 10.7 \mu\text{m}$. Literature data are 3ω measurements on a 520 nm thick film (open squares, Ref. [44]), and thin film microcalorimetry measurements on a 278 nm thick film (open stars, Ref. [45]).

the time constant of the single exponential decay; the thermal conductivity is then computed using the measured heat capacity from Ref. [43]. The maximum grating period used is $15.7 \mu\text{m}$. Within the uncertainty of the measurement, the thermal diffusivity does not vary with grating period above $10.7 \mu\text{m}$, and so we take the value at $10.7 \mu\text{m}$ to be the bulk value. The thermal conductivity versus temperature for $10.7 \mu\text{m}$ is given in Fig. 1C along with literature measurements; each point represents the average of $\sim 10^4$ measurements taken at multiple locations on the membrane. Our measured values are generally in good agreement with prior reports.

The measured TG signal for a grating period of $L = 754 \text{ nm}$ is shown in Fig. 2A. The actual thermal decay is clearly slower than that expected based on the bulk thermal conductivity value, indicating the presence of acoustic excitations with MFPs comparable to the grating period. Measurements of the decay rate versus q^2 for all the grating periods at 80 K are given in Fig. 2B. The measured decay rate is close to that predicted by the

bulk thermal conductivity up to around $q^2 \sim 4.6 \mu\text{m}^{-2}$ ($L \sim 3 \mu\text{m}$), above which the decay rate becomes smaller. The maximum relative deviation in time constant is on the order of 50% as shown in Fig. 2C. Figure 2D shows the measured thermal conductivity versus grating period obtained from these time constants at two of the five temperatures considered in this study. As the grating period becomes comparable to some MFPs, the effective thermal conductivity varies with grating period. The grating period dependence

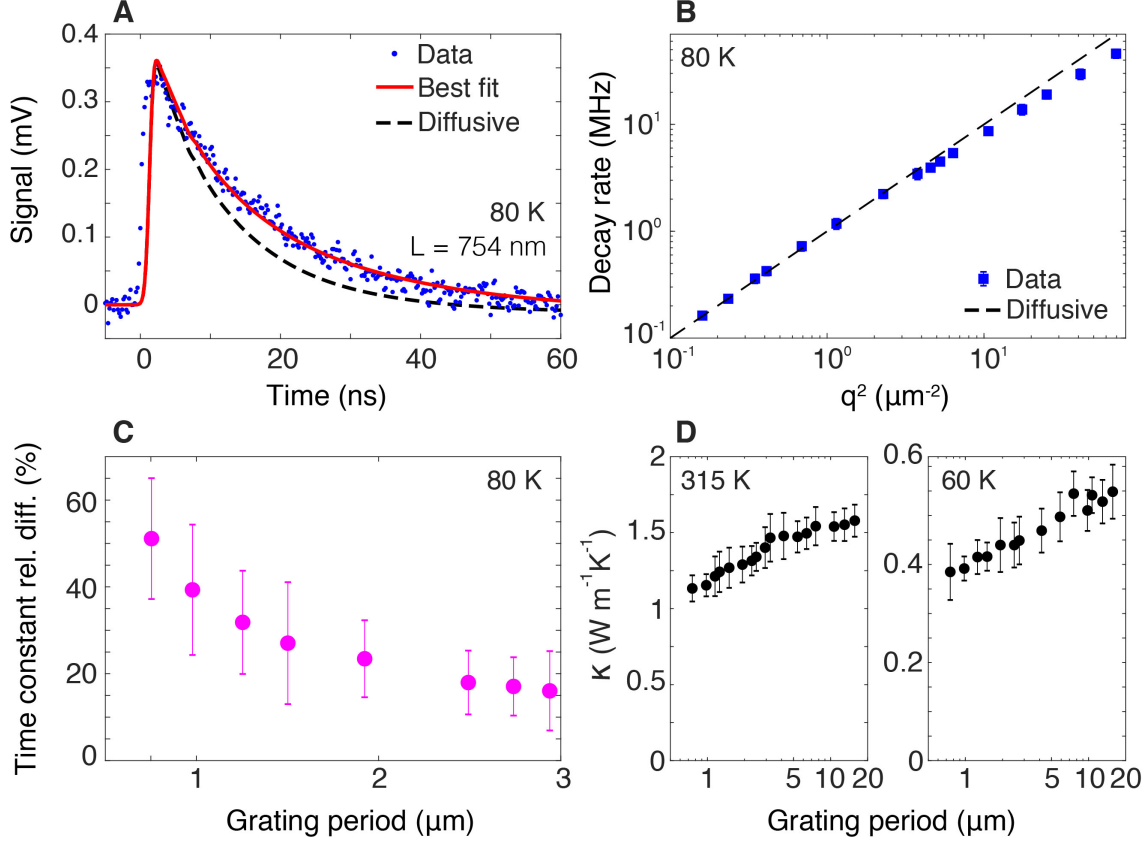


Figure 2. (A) Measured TG signal versus time (symbols) for grating period $L = 754 \text{ nm}$, corresponding to $q^2 \sim 70 \mu\text{m}^{-2}$, along with the best fit (solid red line) and expected decay from diffusion theory (dashed black line). The actual signal decays slower than predicted, indicating a departure from diffusive thermal transport. (B) Inverse time constant versus q^2 . The measured decay rates follow a linear trend of diffusive thermal transport for $q^2 \lesssim 4.6 \mu\text{m}^{-2}$ ($L \gtrsim 3 \mu\text{m}$), above which a clear deviation is observed. (C) Relative difference $(t_{\text{actual}} - t_{\text{bulk}})/t_{\text{bulk}}$ in the thermal decay time constant versus the grating period. (D) Measured thermal conductivity versus grating period at 315 K and 60 K . The thermal conductivity exhibits a dependence on grating period, indicating the presence of heat-carrying acoustic excitations with MFPs comparable to the grating period.

of the thermal conductivity provides constraints on the frequency-dependence of the MFPs of sub-THz excitations. Following Ref. [46], the measured thermal conductivity κ_i can be expressed as

$$\kappa_i = \sum_s \int_0^{\omega_{m,s}} S(x_{i,s}) \left[\frac{1}{3} C_s(\omega) v_s \Lambda_s(\omega) \right] d\omega + \kappa_{IR} \quad (1)$$

where s indexes the polarization, $q_i = 2\pi L_i^{-1}$, $x_{i,s} = q_i \Lambda_s(\omega)$, $S(x_{i,s})$ is the isotropic suppression function in Refs. [46, 47], $\omega_{m,s}$ is the cutoff frequency for collective acoustic excitations, and κ_{IR} is the contribution from excitations above the Ioffe-Regel (IR) cutoff frequency. The Debye heat capacity C_s is calculated from the group velocities v_s which are known, isotropic, and independent of temperature [9, 41]. The first term of Eq. 1 is a Debye model for the thermal conductivity of an isotropic solid that includes the effect of non-diffusive thermal transport over a grating period.

The desired quantity is $\Lambda_s(\omega)$, or the MFP versus frequency for LA and TA polarizations. Additional measurements can be used to further constrain $\Lambda_s(\omega)$ before the TG measurements are used. First, the linewidths of LA excitations at frequencies above 3.7 THz are known from IXS measurements and are independent of temperature [9]. As the TA linewidths are not accessible with IXS, we use the values from MD simulations as they quantitatively agreed with the measurements for the LA branch. These values allow the thermal conductivity of collective excitations above ~ 3.7 THz to be obtained from Eq. 1; at room temperature this contribution is $\sim 0.5 \text{ Wm}^{-1}\text{K}^{-1}$.

Second, the attenuation lengths at hypersonic frequencies can be obtained from picosecond acoustics. The room temperature value is available from Ref. [37]. We performed additional measurements of the acoustic attenuation at temperatures from 30 - 300 K using this method as described in SI Sec. I. The values are on the order of 10 - 20 μm in this temperature range.

The lack of temperature dependence of the damping at both 100 GHz and ~ 3 THz suggests that the MFPs at intermediate frequencies should also be independent of temperature. This requirement, the PSA and IXS measurements, and the measured thermal conductivity versus grating period at the 5 temperatures in this study impose tight constraints on the frequency-dependence of the damping in the sub-THz frequencies. Figure 3A shows two candidate MFP profiles that satisfy these constraints for the LA and TA branches. Power law dependencies $\Lambda \sim \omega^{-n}$ are assumed and combined using Matthiessen's rule. Profile 1

transitions from a constant value to $n = 4$ corresponding to Rayleigh scattering, while profile 2 transitions from constant to $n = 4$ at $\sim 2 - 3$ THz and then to $n = 1$ at $\sim 200 - 300$ GHz.

A representative plot of thermal conductivity versus grating period using Eq. 1 at 60 K is given in Fig. 3B. In this figure, κ_{IR} has been taken as a parameter to give the best fit for each profile. Profile 1 fails to reproduce the trend with grating period. An alternate profile that increases as $n = 4$ immediately at 3.7 THz yields a thermal conductivity that exceeds the experimental values at all temperatures (not shown). We find that only profiles consistent with profile 2 are able to explain the magnitude and grating period dependence of the thermal conductivity. Specifically, the MFPs must remain constant as frequency decreases and then increase rapidly as $n = 4$. To agree with the PSA data, the trend must then switch to $n = 1$ or $n = 2$. From the TG data, we are unable to determine this latter trend owing to the influence of boundary scattering in the 500 nm thick membrane. The specularity parameter required to produce MFPs on the order of microns with this membrane thickness is $\sim 95\%$, a value that is consistent with prior studies of phonons in crystalline Si in this frequency band [48]. For concreteness, we choose $n = 1$ in the following analysis and neglect the influence of boundary scattering.

Given these constraints, the MFPs are characterized by two parameters: the transition frequencies from $n = 4$ to $n = 1$ for both acoustic polarizations, $\omega_{m,L}$ and $\omega_{m,T}$. The remaining unknown parameter is κ_{IR} , which may depend on temperature. We identify the parameters that best explain the TG data by numerically optimizing $\omega_{m,L}$, $\omega_{m,T}$, and $\kappa_{IR}(T)$ to best fit the experimental data. The resulting thermal conductivity versus grating period predicted by Eq. 1 with these parameters at each temperature is shown in Fig. 3, demonstrating good agreement at all temperatures. κ_{IR} versus temperature is given in SI Sec. IV and exhibits the same temperature dependence as the heat capacity, in agreement with the prediction of Allen-Feldman theory [49]. Further discussion of the choices of $\omega_{m,L}$, $\omega_{m,T}$, and κ_{IR} that are compatible with the data is given in SI Sec. V; the trend of MFP with frequency remains the same for all of these parameter sets.

IV. DISCUSSION

The extracted MFPs versus frequency for LA and TA branches are shown in Fig. 4 along with prior measurements on vitreous silica. The trend for aSi agrees well with these and other

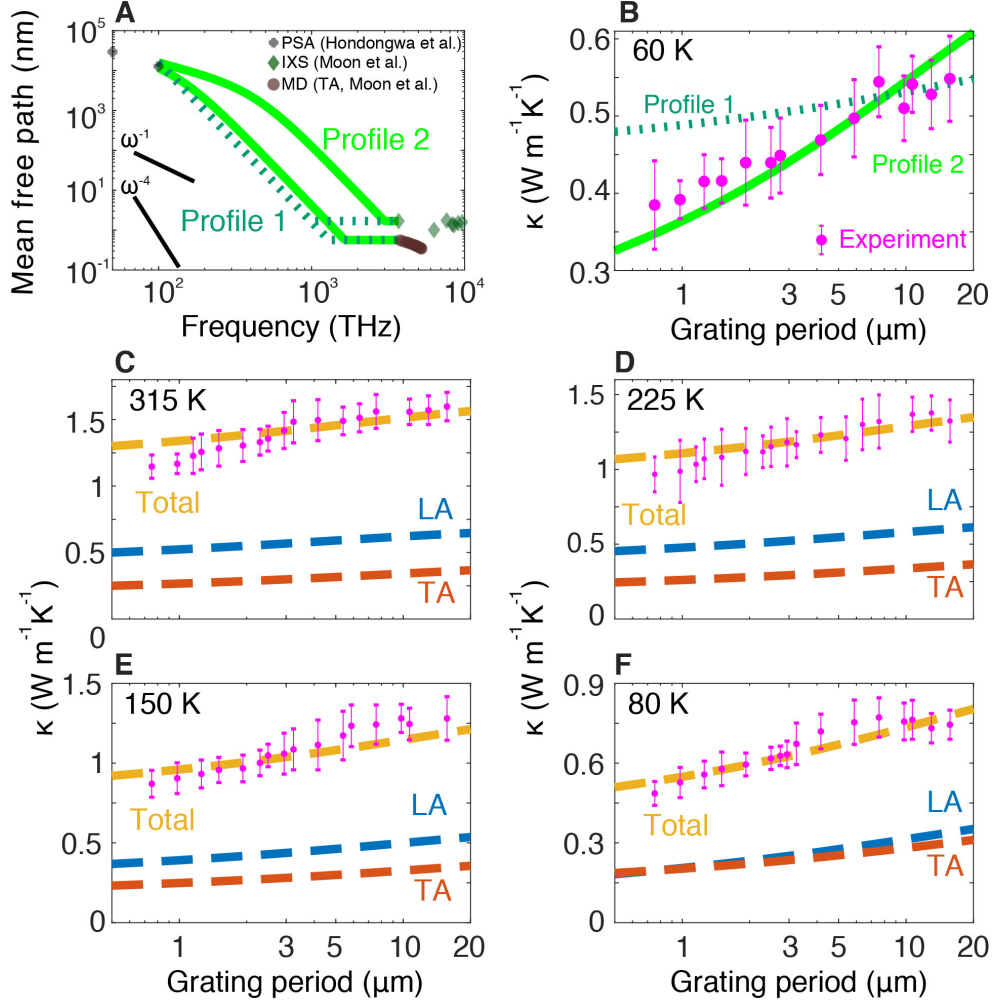


Figure 3. (A) Candidate MFP profiles versus frequency: ω^{-4} , constant (profile 1: green dotted lines); ω^{-1}, ω^{-4} , constant (profile 2: green solid lines). Upper and lower curves indicate the LA and TA MFPs, respectively. Literature data are IXS (diamonds, Ref. [9]), PSA at 300 K (asterisks, Ref. [37]), and molecular dynamics (circles, Ref. [41]) (B) Predicted thermal conductivity versus grating period from each candidate profile along with the measured data at 60 K. Only profile 2 reproduces the trend of the measured thermal conductivity with grating period. Measured thermal conductivity versus grating period (symbols) and predicted value from optimized profile 2 (total, dashed yellow line; LA, dashed blue line; TA, dashed red line) for (C) 315 K, (D) 225 K (E) 150 K (F) 80 K. Good agreement is observed at all temperatures with MFPs that are independent of temperature.

measurements in that similar power-law dependencies are observed [8, 14, 16–19, 24, 50]. The $n = 4$ Rayleigh scattering trend for both glasses occurs in the 1 – 3 THz range with a

transition to a weaker power law in the sub-THz frequencies. Thus qualitatively, acoustic damping in aSi is not so different from those of other glasses.

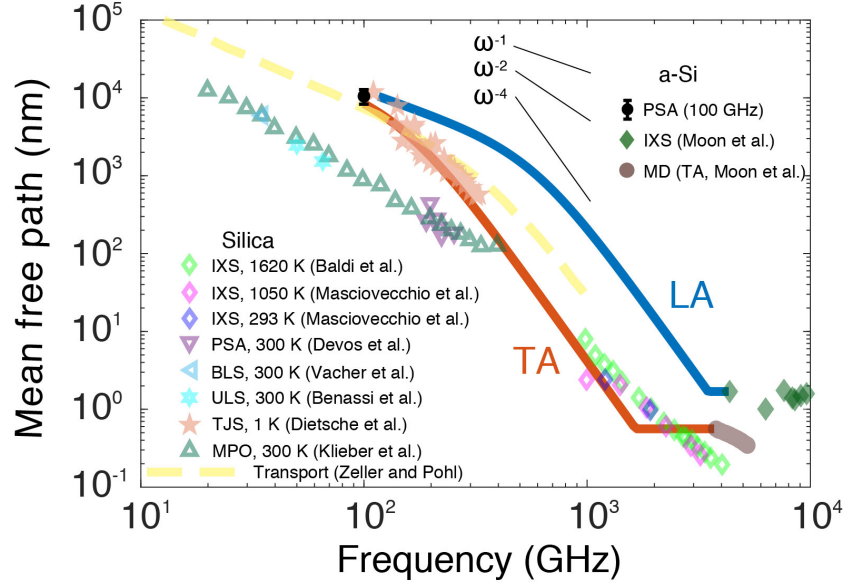


Figure 4. Mean free path versus frequency for thermal acoustic excitations in aSi at 300 K along with literature data for vitreous silica from inelastic x-ray scattering (diamonds, Ref. [8, 12]), picosecond acoustics (downward pointing triangles, Ref. [19]), Brillouin light scattering (left-pointing triangles, Ref. [16] and 6-pointed stars, Ref. [17]), tunnel junction spectroscopy (5-pointed stars, Ref. [14]), a multi-pulse optical technique (upward pointing triangles, Ref. [51]), and from transport measurements (dashed line, Ref. [23]).

However, comparing the attenuation between vitreous silica and aSi, differences also emerge. Comparing the LA MFPs at $\sim 1\text{--}2$ THz, the attenuation due to Rayleigh scattering is weaker in aSi by around a factor of 5, expected as aSi is a monatomic glass with less atomic disorder. Further, at room temperature the $n = 4$ trend yields to a $n \approx 1 - 2$ trend at ~ 700 GHz in vitreous silica while the same transition occurs at $\sim 300 - 400$ GHz in aSi. At cryogenic temperatures ~ 1 K for vitreous silica, the transition frequencies in both materials are comparable. This difference indicates weaker damping by mechanisms such as two-level systems or Akhiezer damping in amorphous Si and has an important consequence: excitations with MFPs in the micron range occur at frequencies of $\sim 200 - 1000$ GHz in aSi versus $\lesssim 100$ GHz in vitreous silica at room temperature owing to the steep $n = 4$ slope of Rayleigh scattering. The heat capacity of excitations in the former frequency range is

larger by a factor of $(\omega_{aSi}/\omega_{SiO_2})^2 \sim 100$. The result is that in aSi, heat-carrying excitations at room temperature have micron-scale MFPs, while the MFPs of excitations in the same frequency band for vitreous silica are smaller by an order of magnitude. Excitations in vitreous silica with micron-scale MFPs have too low frequency to transport substantial heat at room temperature. Remarkably, the attenuation observed in aSi up to room temperature is of the same order as that measured in vitreous silica at 1 K, highlighting the unusually weak acoustic damping in aSi.

Our conclusions on the origin of damping of sub-THz excitations in aSi are consistent with these prior studies of other glasses, and the extracted $\kappa_{IR}(T)$ for excitations above the IR frequency is compatible with Allen-Feldman theory. However, our results are not consistent with the conclusions of numerical studies of excitations below the IR frequency [34–36, 52, 53]. In these studies, the Hamiltonian for atoms in a supercell is diagonalized in the harmonic approximation to yield normal modes. The original studies of Allen and Feldman used these normal modes to classify excitations in glasses as propagons, diffusons, and locons depending on the properties of the eigenvectors [54]. The lifetimes of these modes are obtained using normal mode decomposition and molecular dynamics [55, 56]. With these approaches, these studies have generally concluded that damping in aSi varies as ω^{-2} for frequencies around $\sim 1 - 2$ THz and below. From this trend, the damping mechanism has been postulated to involve anharmonicity [35, 36] and to exhibit a temperature dependence [34].

We first address the classification of acoustic excitations. Various numerical [33–35] and experimental works [32] have noted a transition in the character of vibrations in aSi around $\sim 1 - 2$ THz, leading to the introduction of “diffusons” as non-propagating yet delocalized vibrations in Refs. [33, 34]. In contrast, our work attributes this change to a frequency-dependent damping of collective acoustic excitations. The crossover from propagons and diffusons at $\sim 1 - 2$ THz coincides with the transition from Rayleigh scattering to the Kittel regime in the present work and thus can be explained without the definition of a new type of vibration. The IR crossover for the transition from collective excitations to incoherent excitations, which occurs well above 1-2 THz in amorphous Si, is sufficient to describe the different characters of excitations in glasses.

The second inconsistency is the prediction by normal-mode analysis of the frequency-dependence ($n = 2$) and anharmonic origin of damping in the few THz frequency range.

Specifically, the MFPs predicted from normal mode analysis are on the order of 20 nm at ~ 1 THz (smaller by factor of 5 compared to present value of ~ 100 nm) and vary as ω^{-2} (see Fig. 4B of Ref. [35]), which cannot explain the measurements of the present work. Here, the inconsistency appears to arise from the implicit assumption of the normal mode decomposition that the heat-carrying excitations in glasses are the normal modes of the supercell. This assumption is not compatible with basic many-body physics and scattering theory, which instead gives the proper definition and lifetime of a collective excitation of a many-body system using the self-energy and the single-particle Green's function [57]. Rather than normal modes, a physical picture of acoustic excitations of a glass that is compatible with this framework is that originally postulated by Kittel [20] in the continuum limit and later by Zeller and Pohl [23], in which a glass is imagined to consist of a fictitious atomic lattice along with perturbations representing the mass and force constant disorder in the actual glass. The undamped excitations of the fictitious atomic lattice acquire a lifetime owing to the disorder of the actual glass. The dispersion and lifetimes of these excitations can be measured experimentally using inelastic scattering, as has been performed for many glasses in the past decades [8–13]. In contrast, the lifetimes of normal modes do not appear to be experimentally accessible or physically meaningful as they are unable to explain the thermal conductivity measurements presented here.

V. SUMMARY

In summary, we have obtained measurements of the frequency-dependent MFPs of sub-THz acoustic excitations in amorphous silicon using picosecond acoustics and transient grating spectroscopy. The MFPs lack a temperature dependence and exhibit a trend characteristic of structural scattering by point defects and density fluctuations. This result is at variance with numerical studies based on normal mode analysis but is broadly consistent with prior studies of vitreous silica and other glasses. The micron-scale MFPs of heat-carrying excitations at room temperature are found to arise primarily from the weak anharmonic and two-level system damping of sub-THz excitations, leading to room temperature attenuation coefficients comparable to those of other glasses at cryogenic temperatures.

ACKNOWLEDGMENTS

The authors acknowledge discussions with A. B. Robbins and B. C. Daly. This work was supported by the 2018 GIST-Caltech Research Collaboration.

- [1] V. K Malinovsky, V. N Novikov, P. P Parshin, A. P Sokolov, and M. G Zemlyanov. Universal form of the low-energy (2 to 10 meV) vibrational spectrum of glasses. *Europhysics Letters (EPL)*, 11(1):43–47, jan 1990. doi:10.1209/0295-5075/11/1/008. URL <https://doi.org/10.1209%2F0295-5075%2F11%2F1%2F008>.
- [2] X Liu and H. v Löhneysen. Specific-heat anomaly of amorphous solids at intermediate temperatures (1 to 30 k). *Europhysics Letters (EPL)*, 33(8):617–622, mar 1996. doi:10.1209/epl/i1996-00388-9. URL <https://doi.org/10.1209%2Fep1%2Fi1996-00388-9>.
- [3] J. Jäckle, L. Piché, W. Arnold, and S. Hunklinger. Elastic effects of structural relaxation in glasses at low temperatures. *Journal of Non-Crystalline Solids*, 20(3):365–391, May 1976. ISSN 0022-3093. doi:10.1016/0022-3093(76)90119-8. URL <http://www.sciencedirect.com/science/article/pii/0022309376901198>.
- [4] W. A. Phillips. Tunneling states in amorphous solids. *Journal of Low Temperature Physics*, 7(3):351–360, 1972. doi:10.1007/BF00660072. URL <https://doi.org/10.1007/BF00660072>.
- [5] S. HUNKLINGER and W. ARNOLD. 3 - ultrasonic properties of glasses at low temperatures. volume 12 of *Physical Acoustics*, pages 155 – 215. Academic Press, 1976. doi:https://doi.org/10.1016/B978-0-12-477912-9.50008-4. URL <http://www.sciencedirect.com/science/article/pii/B9780124779129500084>.
- [6] P. W. Anderson, B. I. Halperin, and C. M. Varma. Anomalous low-temperature thermal properties of glasses and spin glasses. *The Philosophical Magazine: A Journal of Theoretical Experimental and Applied Physics*, 25(1):1–9, 1972. doi:10.1080/14786437208229210. URL <https://doi.org/10.1080/14786437208229210>.
- [7] M. P. Zaitlin and A. C. Anderson. An explanation for the plateau in the thermal conductivity of non-crystalline solids. *physica status solidi (b)*, 71(1):323–327, 1975. doi:10.1002/pssb.2220710132. URL <https://onlinelibrary.wiley.com/doi/abs/10.1002/pssb.2220710132>.

- [8] G. Baldi, V. M. Giordano, G. Monaco, and B. Ruta. Sound Attenuation at Terahertz Frequencies and the Boson Peak of Vitreous Silica. *Physical Review Letters*, 104(19):195501, May 2010. doi:10.1103/PhysRevLett.104.195501. URL <https://link.aps.org/doi/10.1103/PhysRevLett.104.195501>.
- [9] Jaeyun Moon, Raphaël P. Hermann, Michael E. Manley, Ahmet Alatas, Ayman H. Said, and Austin J. Minnich. Thermal acoustic excitations with atomic-scale wavelengths in amorphous silicon. *Phys. Rev. Materials*, 3:065601, Jun 2019. doi:10.1103/PhysRevMaterials.3.065601. URL <https://link.aps.org/doi/10.1103/PhysRevMaterials.3.065601>.
- [10] Giulio Monaco and Valentina M. Giordano. Breakdown of the Debye approximation for the acoustic modes with nanometric wavelengths in glasses. *Proceedings of the National Academy of Sciences*, 106(10):3659–3663, March 2009. ISSN 0027-8424, 1091-6490. doi:10.1073/pnas.0808965106. URL <https://www.pnas.org/content/106/10/3659>.
- [11] B. Rufflé, G. Guimbretière, E. Courtens, R. Vacher, and G. Monaco. Glass-specific behavior in the damping of acousticlike vibrations. *Phys. Rev. Lett.*, 96:045502, Jan 2006. doi:10.1103/PhysRevLett.96.045502. URL <https://link.aps.org/doi/10.1103/PhysRevLett.96.045502>.
- [12] C. Masciovecchio, G. Ruocco, F. Sette, M. Krisch, R. Verbeni, U. Bergmann, and M. Soltwisch. Observation of large momentum phononlike modes in glasses. *Phys. Rev. Lett.*, 76:3356–3359, Apr 1996. doi:10.1103/PhysRevLett.76.3356. URL <https://link.aps.org/doi/10.1103/PhysRevLett.76.3356>.
- [13] Francesco Sette, Michael H. Krisch, Claudio Masciovecchio, Giancarlo Ruocco, and Giulio Monaco. Dynamics of glasses and glass-forming liquids studied by inelastic x-ray scattering. *Science*, 280(5369):1550–1555, 1998. ISSN 0036-8075. doi:10.1126/science.280.5369.1550. URL <https://science.sciencemag.org/content/280/5369/1550>.
- [14] W. Dietsche and H. Kinder. Spectroscopy of Phonon Scattering in Glass. *Physical Review Letters*, 43(19):1413–1417, November 1979. doi:10.1103/PhysRevLett.43.1413. URL <https://link.aps.org/doi/10.1103/PhysRevLett.43.1413>.
- [15] R. Vacher, H. Sussner, and S. Hunklinger. Brillouin scattering in vitreous silica below 1 k. *Phys. Rev. B*, 21:5850–5853, Jun 1980. doi:10.1103/PhysRevB.21.5850. URL <https://link.aps.org/doi/10.1103/PhysRevB.21.5850>.

- [16] R. Vacher and J. Pelous. Behavior of thermal phonons in amorphous media from 4 to 300 k. *Phys. Rev. B*, 14:823–828, Jul 1976. doi:10.1103/PhysRevB.14.823. URL <https://link.aps.org/doi/10.1103/PhysRevB.14.823>.
- [17] P. Benassi, S. Caponi, R. Eramo, A. Fontana, A. Giugni, M. Nardone, M. Sampoli, and G. Viliani. Sound attenuation in a unexplored frequency region: Brillouin ultraviolet light scattering measurements in v -SiO₂. *Phys. Rev. B*, 71:172201, May 2005. doi:10.1103/PhysRevB.71.172201. URL <https://link.aps.org/doi/10.1103/PhysRevB.71.172201>.
- [18] T. C. Zhu, H. J. Maris, and J. Tauc. Attenuation of longitudinal-acoustic phonons in amorphous sio₂ at frequencies up to 440 ghz. *Phys. Rev. B*, 44:4281–4289, Sep 1991. doi:10.1103/PhysRevB.44.4281. URL <https://link.aps.org/doi/10.1103/PhysRevB.44.4281>.
- [19] A. Devos, M. Foret, S. Ayrinhac, P. Emery, and B. Rufflé. Hypersound damping in vitreous silica measured by picosecond acoustics. *Phys. Rev. B*, 77:100201, Mar 2008. doi:10.1103/PhysRevB.77.100201. URL <https://link.aps.org/doi/10.1103/PhysRevB.77.100201>.
- [20] Charles Kittel. Interpretation of the thermal conductivity of glasses. *Phys. Rev.*, 75:972–974, Mar 1949. doi:10.1103/PhysRev.75.972. URL <https://link.aps.org/doi/10.1103/PhysRev.75.972>.
- [21] J. J. Freeman and A. C. Anderson. Thermal conductivity of amorphous solids. *Phys. Rev. B*, 34:5684–5690, Oct 1986. doi:10.1103/PhysRevB.34.5684. URL <https://link.aps.org/doi/10.1103/PhysRevB.34.5684>.
- [22] K. E. Goodson, M. I. Flik, L. T. Su, and D. A. Antoniadis. Prediction and Measurement of the Thermal Conductivity of Amorphous Dielectric Layers. *Journal of Heat Transfer*, 116(2):317–324, 05 1994. ISSN 0022-1481. doi:10.1115/1.2911402. URL <https://doi.org/10.1115/1.2911402>.
- [23] R. C. Zeller and R. O. Pohl. Thermal conductivity and specific heat of noncrystalline solids. *Phys. Rev. B*, 4:2029–2041, Sep 1971. doi:10.1103/PhysRevB.4.2029. URL <https://link.aps.org/doi/10.1103/PhysRevB.4.2029>.
- [24] J. E. Graebner, B. Golding, and L. C. Allen. Phonon localization in glasses. *Phys. Rev. B*, 34:5696–5701, Oct 1986. doi:10.1103/PhysRevB.34.5696. URL <https://link.aps.org/doi/10.1103/PhysRevB.34.5696>.

- 10.1103/PhysRevB.34.5696.
- [25] M. Von Haumer, U. Strom, and S. Hunklinger. Acoustic Anomalies in Amorphous Thin Films of Si and SiO₂. *Physical Review Letters*, 44(2):84–87, January 1980. doi:10.1103/PhysRevLett.44.84. URL <https://link.aps.org/doi/10.1103/PhysRevLett.44.84>.
 - [26] Xiao Liu, B. E. White, Jr., R. O. Pohl, E. Iwanizcko, K. M. Jones, A. H. Mahan, B. N. Nelson, R. S. Crandall, and S. Veprek. Amorphous solid without low energy excitations. *Phys. Rev. Lett.*, 78:4418–4421, Jun 1997. doi:10.1103/PhysRevLett.78.4418. URL <https://link.aps.org/doi/10.1103/PhysRevLett.78.4418>.
 - [27] L. Wiczorek, H. J. Goldsmid, and G. L. Paul. *Thermal Conductivity of Amorphous Films*, pages 235–241. Springer US, Boston, MA, 1989. ISBN 978-1-4613-0761-7. doi:10.1007/978-1-4613-0761-7_22. URL https://doi.org/10.1007/978-1-4613-0761-7_22.
 - [28] B. S. W. Kuo, J. C. M. Li, and A. W. Schmid. Thermal conductivity and interface thermal resistance of si film on si substrate determined by photothermal displacement interferometry. *Applied Physics A*, 55(3):289–296, 1992. doi:10.1007/BF00348399. URL <https://doi.org/10.1007/BF00348399>.
 - [29] Seungjae Moon, Mutsuko Hatano, Minghong Lee, and Costas P. Grigoropoulos. Thermal conductivity of amorphous silicon thin films. *International Journal of Heat and Mass Transfer*, 45(12):2439–2447, June 2002. ISSN 00179310. doi:10.1016/S0017-9310(01)00347-7. URL <http://linkinghub.elsevier.com/retrieve/pii/S0017931001003477>.
 - [30] Xiao Liu, J. L. Feldman, D. G. Cahill, R. S. Crandall, N. Bernstein, D. M. Photiadis, M. J. Mehl, and D. A. Papaconstantopoulos. High thermal conductivity of a hydrogenated amorphous silicon film. *Phys. Rev. Lett.*, 102:035901, Jan 2009. doi:10.1103/PhysRevLett.102.035901. URL <https://link.aps.org/doi/10.1103/PhysRevLett.102.035901>.
 - [31] Soonshin Kwon, Jianlin Zheng, Matthew C. Wingert, Shuang Cui, and Renkun Chen. Unusually high and anisotropic thermal conductivity in amorphous silicon nanostructures. *ACS Nano*, 11(3):2470–2476, 2017. doi:10.1021/acsnano.6b07836. URL <https://doi.org/10.1021/acsnano.6b07836>. PMID: 28117979.
 - [32] Jeffrey L. Braun, Christopher H. Baker, Ashutosh Giri, Mirza Elahi, Kateryna Artyushkova, Thomas E. Beechem, Pamela M. Norris, Zayd C. Leseman, John T. Gaskins, and Patrick E.

- Hopkins. Size effects on the thermal conductivity of amorphous silicon thin films. *Phys. Rev. B*, 93:140201, Apr 2016. doi:10.1103/PhysRevB.93.140201. URL <https://link.aps.org/doi/10.1103/PhysRevB.93.140201>.
- [33] Philip B. Allen, Joseph L. Feldman, Jaroslav Fabian, and Frederick Wooten. Diffusons, locons and propagons: Character of atomic vibrations in amorphous si. *Philosophical Magazine B*, 79 (11-12):1715–1731, 1999. doi:10.1080/13642819908223054. URL <https://doi.org/10.1080/13642819908223054>.
- [34] Jaroslav Fabian and Philip B. Allen. Anharmonic decay of vibrational states in amorphous silicon. *Phys. Rev. Lett.*, 77:3839–3842, Oct 1996. doi:10.1103/PhysRevLett.77.3839. URL <https://link.aps.org/doi/10.1103/PhysRevLett.77.3839>.
- [35] Jason M. Larkin and Alan J. H. McGaughey. Thermal conductivity accumulation in amorphous silica and amorphous silicon. *Phys. Rev. B*, 89:144303, Apr 2014. doi:10.1103/PhysRevB.89.144303. URL <https://link.aps.org/doi/10.1103/PhysRevB.89.144303>.
- [36] K. Sääskilähti, J. Oksanen, J. Tulkki, A. J. H. McGaughey, and S. Volz. Vibrational mean free paths and thermal conductivity of amorphous silicon from non-equilibrium molecular dynamics simulations. *AIP Advances*, 6(12):121904, 2016. doi:10.1063/1.4968617. URL <https://doi.org/10.1063/1.4968617>.
- [37] D. B. Hondongwa, B. C. Daly, T. B. Norris, B. Yan, J. Yang, and S. Guha. Ultrasonic attenuation in amorphous silicon at 50 and 100 ghz. *Phys. Rev. B*, 83:121303, Mar 2011. doi:10.1103/PhysRevB.83.121303. URL <https://link.aps.org/doi/10.1103/PhysRevB.83.121303>.
- [38] Jeremy A. Johnson, A. A. Maznev, John Cuffe, Jeffrey K. Eliason, Austin J. Minnich, Timothy Kehoe, Clivia M. Sotomayor Torres, Gang Chen, and Keith A. Nelson. Direct measurement of room-temperature nondiffusive thermal transport over micron distances in a silicon membrane. *Phys. Rev. Lett.*, 110:025901, Jan 2013. doi:10.1103/PhysRevLett.110.025901. URL <https://link.aps.org/doi/10.1103/PhysRevLett.110.025901>.
- [39] Navaneetha K. Ravichandran, Hang Zhang, and Austin J. Minnich. Spectrally resolved specular reflections of thermal phonons from atomically rough surfaces. *Phys. Rev. X*, 8: 041004, Oct 2018. doi:10.1103/PhysRevX.8.041004. URL <https://link.aps.org/doi/10.1103/PhysRevX.8.041004>.

- [40] Andrew B. Robbins, Stavros X. Drakopoulos, Ignacio Martin-Fabiani, Sara Ronca, and Austin J. Minnich. Ballistic thermal phonons traversing nanocrystalline domains in oriented polyethylene. *Proceedings of the National Academy of Sciences*, 116(35):17163–17168, 2019. ISSN 0027-8424. doi:10.1073/pnas.1905492116. URL <https://www.pnas.org/content/116/35/17163>.
- [41] Jaeyun Moon, Benoit Latour, and Austin J. Minnich. Propagating elastic vibrations dominate thermal conduction in amorphous silicon. *Phys. Rev. B*, 97:024201, Jan 2018. doi:10.1103/PhysRevB.97.024201. URL <https://link.aps.org/doi/10.1103/PhysRevB.97.024201>.
- [42] A. A. Maznev, K. A. Nelson, and J. A. Rogers. Optical heterodyne detection of laser-induced gratings. *Opt. Lett.*, 23(16):1319–1321, Aug 1998. doi:10.1364/OL.23.001319. URL <http://ol.osa.org/abstract.cfm?URI=ol-23-16-1319>.
- [43] D. R. Queen, X. Liu, J. Karel, T. H. Metcalf, and F. Hellman. Excess specific heat in evaporated amorphous silicon. *Phys. Rev. Lett.*, 110:135901, Mar 2013. doi:10.1103/PhysRevLett.110.135901. URL <https://link.aps.org/doi/10.1103/PhysRevLett.110.135901>.
- [44] David G. Cahill, M. Katiyar, and J. R. Abelson. Thermal conductivity of a-si:h thin films. *Phys. Rev. B*, 50:6077–6081, Sep 1994. doi:10.1103/PhysRevB.50.6077. URL <https://link.aps.org/doi/10.1103/PhysRevB.50.6077>.
- [45] B. L. Zink, R. Pietri, and F. Hellman. Thermal conductivity and specific heat of thin-film amorphous silicon. *Phys. Rev. Lett.*, 96:055902, Feb 2006. doi:10.1103/PhysRevLett.96.055902. URL <https://link.aps.org/doi/10.1103/PhysRevLett.96.055902>.
- [46] A. J. Minnich. Determining phonon mean free paths from observations of quasiballistic thermal transport. *Phys. Rev. Lett.*, 109:205901, Nov 2012. doi:10.1103/PhysRevLett.109.205901. URL <https://link.aps.org/doi/10.1103/PhysRevLett.109.205901>.
- [47] A. A. Maznev, Jeremy A. Johnson, and Keith A. Nelson. Onset of nondiffusive phonon transport in transient thermal grating decay. *Phys. Rev. B*, 84:195206, Nov 2011. doi:10.1103/PhysRevB.84.195206. URL <https://link.aps.org/doi/10.1103/PhysRevB.84.195206>.

- [48] Tom Klitsner and R. O. Pohl. Phonon scattering at silicon crystal surfaces. *Phys. Rev. B*, 36:6551–6565, Oct 1987. doi:10.1103/PhysRevB.36.6551. URL <https://link.aps.org/doi/10.1103/PhysRevB.36.6551>.
- [49] Philip B. Allen and Joseph L. Feldman. Thermal conductivity of disordered harmonic solids. *Phys. Rev. B*, 48:12581–12588, Nov 1993. doi:10.1103/PhysRevB.48.12581. URL <https://link.aps.org/doi/10.1103/PhysRevB.48.12581>.
- [50] M. P. Zaitlin and A. C. Anderson. Phonon thermal transport in noncrystalline materials. *Phys. Rev. B*, 12:4475–4486, Nov 1975. doi:10.1103/PhysRevB.12.4475. URL <https://link.aps.org/doi/10.1103/PhysRevB.12.4475>.
- [51] C. Klieber, E. Peronne, K. Katayama, J. Choi, M. Yamaguchi, T. Pezeril, and Keith A. Nelson. Narrow-band acoustic attenuation measurements in vitreous silica at frequencies between 20 and 400 ghz. *Applied Physics Letters*, 98(21):211908, 2011. doi:10.1063/1.3595275. URL <https://doi.org/10.1063/1.3595275>.
- [52] Yuping He, Davide Donadio, and Giulia Galli. Heat transport in amorphous silicon: Interplay between morphology and disorder. *Applied Physics Letters*, 98(14):144101, 2011. doi:10.1063/1.3574366. URL <https://doi.org/10.1063/1.3574366>.
- [53] Jaroslav Fabian and Philip B. Allen. Theory of sound attenuation in glasses: The role of thermal vibrations. *Phys. Rev. Lett.*, 82:1478–1481, Feb 1999. doi:10.1103/PhysRevLett.82.1478. URL <https://link.aps.org/doi/10.1103/PhysRevLett.82.1478>.
- [54] Joseph L. Feldman, Mark D. Kluge, Philip B. Allen, and Frederick Wooten. Thermal conductivity and localization in glasses: Numerical study of a model of amorphous silicon. *Phys. Rev. B*, 48:12589–12602, Nov 1993. doi:10.1103/PhysRevB.48.12589. URL <https://link.aps.org/doi/10.1103/PhysRevB.48.12589>.
- [55] Anthony J. C. Ladd, Bill Moran, and William G. Hoover. Lattice thermal conductivity: A comparison of molecular dynamics and anharmonic lattice dynamics. *Phys. Rev. B*, 34:5058–5064, Oct 1986. doi:10.1103/PhysRevB.34.5058. URL <https://link.aps.org/doi/10.1103/PhysRevB.34.5058>.
- [56] A. J. H. McGaughey and M. Kaviani. Quantitative validation of the boltzmann transport equation phonon thermal conductivity model under the single-mode relaxation time approximation. *Phys. Rev. B*, 69:094303, Mar 2004. doi:10.1103/PhysRevB.69.094303. URL <https://link.aps.org/doi/10.1103/PhysRevB.69.094303>.

- [57] Piers Coleman. *Introduction to Many-Body Physics*. Cambridge University Press, 2015. doi: 10.1017/CBO9781139020916. URL <https://doi.org/10.1017/CBO9781139020916>.

Supporting information: Origin of micron-scale propagation lengths of heat-carrying acoustic excitations in amorphous silicon

Taeyong Kim,¹ Jaeyun Moon,^{2,3} and Austin J. Minnich^{1,*}

¹*Division of Engineering and Applied Science,
California Institute of Technology, Pasadena, California 91125, USA*

²*Department of Materials Science and Engineering,
University of Tennessee, Knoxville, Tennessee 37996, USA*

³*Shull Wollan Center—a Joint Institute for Neutron Sciences,
Oak Ridge National Laboratory, Oak Ridge, Tennessee 37831, USA*

(Dated: March 4, 2024)

I. PICOSECOND ACOUSTICS (PSA)

The attenuation coefficient of hypersonic waves in aSi films on sapphire substrates was measured using picosecond acoustics (PSA). The samples were prepared using the same method as in the main text except with a sapphire substrate (University wafer) and a variable deposition time to prepare three samples with different thicknesses: ~ 500 nm, ~ 1 μ m, and ~ 4 μ m. A 15 nm layer of Al is deposited afterwards by electron beam evaporation to serve as a transducer.

The optical system used for PSA is identical to that used in time domain thermoreflectance (TDTR). Briefly, a train of the pulses (repetition rate: 76 MHz, wavelength 785 nm) is split into pump ($1/e^2$ diameter: 13.7 μ m, power: ~ 10 mW) and probe ($1/e^2$ diameter: 12.4 μ m, power: ~ 3 mW) using a two-tint color method [1]. The pump is amplitude-modulated at 9.2 MHz and focused onto the sample. The pump absorption induces a thermal expansion of the Al transducer, thermoelastically launching a longitudinal strain pulse. A 15 nm Al film was chosen as a transducer to generate an acoustic of pulse around $\sim 100 \pm 20$ GHz that propagates through the aSi as in Ref. [2]. The strain pulse experiences multiple reflections between Al transducer and the sapphire substrate, producing changes in reflectance of the transducer film. Sapphire was chosen as a substrate to enhance the magnitude of the echo signals based on the acoustic mismatch model [2] (for sapphire, $\rho = 3.98$ g cm^{-3} , $v_{LA} \sim 11000$ m s^{-1}) [3]. The resulting signal is detected using a lock-in amplifier.

* aminnich@caltech.edu

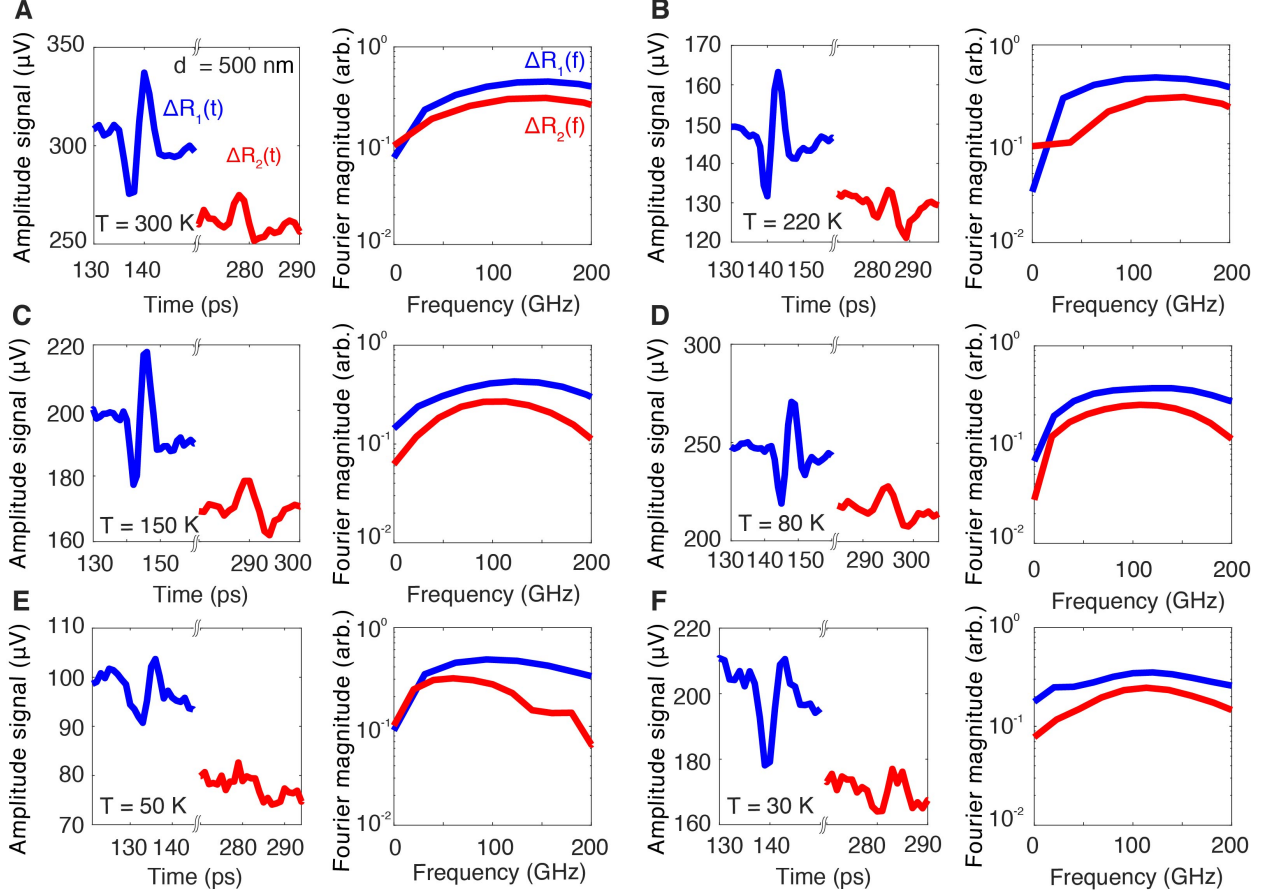


Figure S1. (A) (Left) Measured amplitude signal from ~ 500 nm aSi versus delay time using picosecond acoustics at 300 K. The thermal background signals have been removed. Echo 1 occurs at the Al transducer after a round trip between the transducer and the substrate. The echo 2 is the attenuated signal from echo 1 after one more round trip. The thickness of the aSi film was determined from the time difference between the echoes and the known LA sound velocity. (Right) Fast Fourier transform (FFT) magnitude of echo 1 and echo 2 at 300 K. The peak of the FFT for the first echo occurs at ~ 100 GHz, indicating that 15 nm Al transducer can generate acoustic waves with frequency ~ 100 GHz as expected. Note the attenuation for the 500 nm film is due to the reflection or interface loss at the boundary between the aSi and the sapphire. Amplitude signal along with the corresponding magnitude of the Fourier transform measured at (B) 220 K, (C) 150 K, (D) 80 K, (E) 50 K, and (F) 30 K.

The amplitude signal versus the delay time for ~ 500 nm and ~ 4 μm samples are plotted in Figs. S1 and S2. The resultant magnitude of the signal after one (two) round trip(s) are shown as $\Delta R_1(t)$ ($\Delta R_2(t)$). Following Ref. [2], we analyze the data using Fourier analysis. First, we remove the background signal in $\Delta R_1(t)$ and $\Delta R_2(t)$. Then, $\Delta R_2(t)$ is normalized by the maximum magnitude of $\Delta R_1(t)$. Next, the signals are zero-padded to improve the frequency resolution of the fast Fourier transform (FFT). Finally, the time domain signals are windowed using a Hann

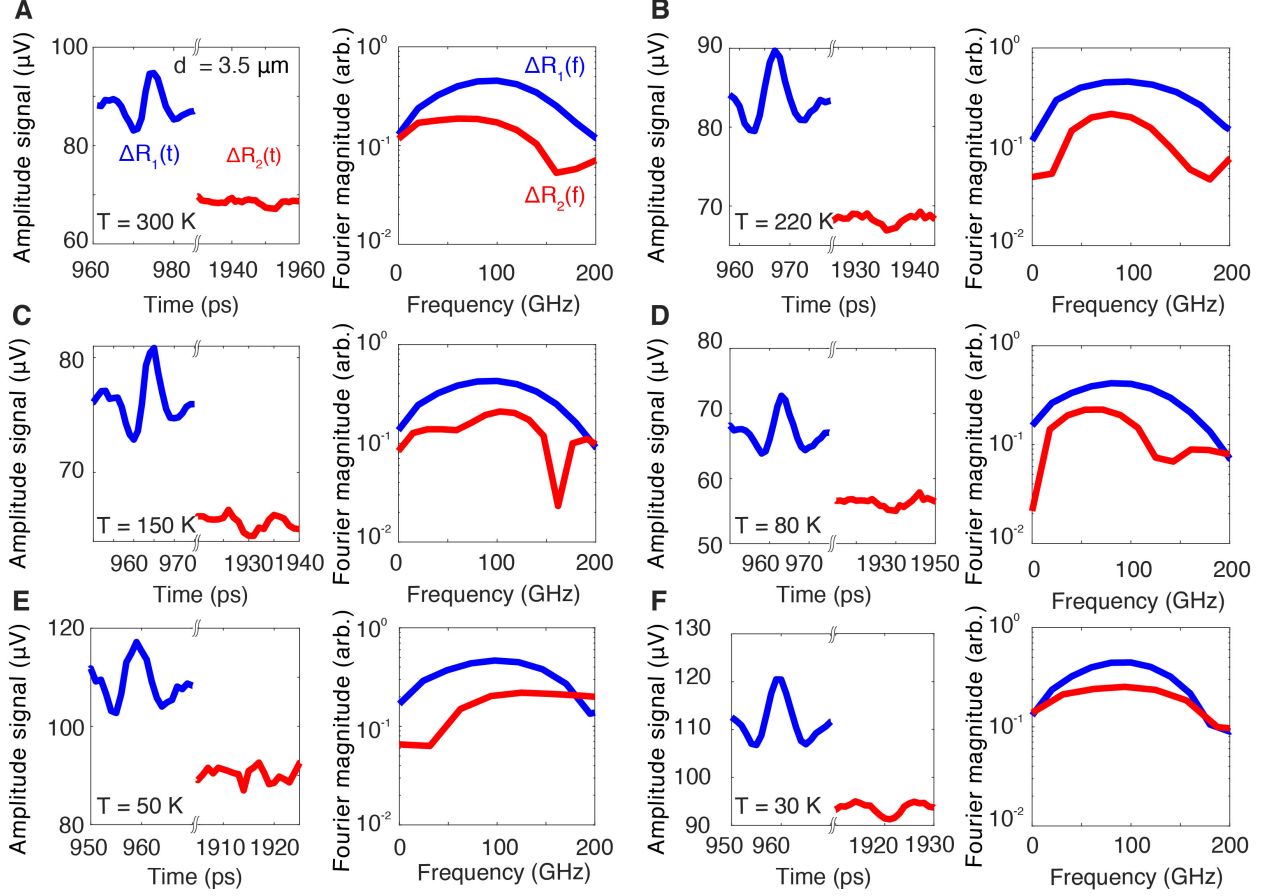


Figure S2. (Left) Measured thermoreflectance signal from $4 \mu\text{m}$ sample versus delay time using picosecond acoustics at (A) 300 K, (B) 220 K, (C) 150 K, (D) 80 K, (E) 50 K, and (F) 30 K. The thermal background has been removed. (Right) Magnitude of Fourier transform of echo 1 and echo 2 at the same temperatures.

window and the FFT is performed.

The resulting Fourier power spectra of each echo are plotted in Figs. S1 and S2. The peak of the FFT occurs at ~ 100 GHz, indicating that 15 nm Al transducer can generate acoustic wave with a frequency ~ 100 GHz as expected. Despite a slight frequency dependence described in Ref. [4], following Ref. [2, 4, 5], rather than treating each Fourier amplitude separately, we compare Fourier amplitude at 100 GHz in Fig. S3A. As in Ref. [2], we find that the ratio of the Fourier magnitude at 100 GHz for 500 nm thickness is close to what is predicted by acoustic mismatch model (AMM) between aSi and the sapphire, $r = (\rho_{\text{sapphire}} v_{\text{sapphire}} - \rho_{\text{aSi}} v_{\text{aSi}}) / (\rho_{\text{sapphire}} v_{\text{sapphire}} + \rho_{\text{aSi}} v_{\text{aSi}}) = 0.42 = 2.4^{-1}$, indicating that the loss for 500 nm thickness is dominated by transmission into the sapphire substrate.

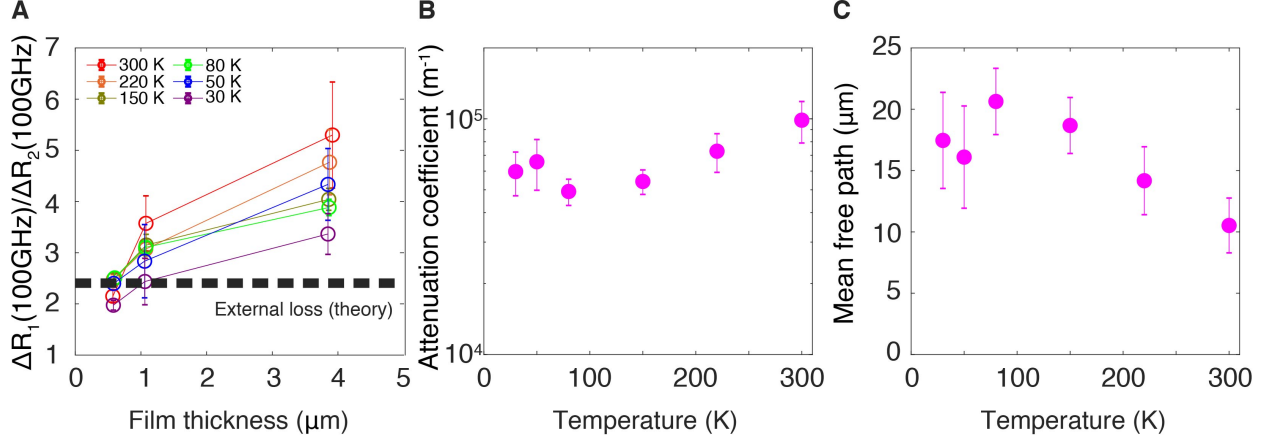


Figure S3. (A) Ratio of the Fourier magnitude at 100 GHz measured at temperatures from 30 K to 300 K. The black dashed line indicates the predicted loss at the boundary between aSi and the sapphire from the AMM. Following Ref. [2], external losses were experimentally deduced from the ratio at ~ 500 nm. Internal damping was obtained from the values at $\sim 4 \mu\text{m}$ using Eq. S1. The film thicknesses were obtained from the time difference between the echoes. The error bar indicates standard deviation determined from multiple measurements. (B) Attenuation coefficients versus temperature using the 500 nm data for reflection loss and $\sim 4 \mu\text{m}$ data for attenuation. (C) Mean free path versus temperature for the 100 GHz vibrations.

The attenuation coefficient for 100 GHz vibrations is obtained from

$$\alpha = \frac{1}{d} \ln \left(\frac{r \Delta R_1(\omega)}{\Delta R_2(\omega)} \right) \quad (\text{S1})$$

where d is the round trip distance, r is the inverse of the value from 500 nm aSi in Fig. S3A, and $\Delta R_1(\omega)/\Delta R_2(\omega)$ is the value from the $4 \mu\text{m}$ thickness sample in Fig. S3A.

The calculated attenuation coefficient is shown in Fig. S3B. The measured coefficient is $\sim 10^2 - 10^3 \text{ cm}^{-1}$ with its maximum value at 300 K ($987 \pm 197 \text{ cm}^{-1}$). The measured value at room temperature is close to that reported from PSA in aSi ($780 \pm 160 \text{ cm}^{-1}$) [2] but substantially lower than that of vitreous silica ($\sim 10000 \text{ cm}^{-1}$ at ~ 100 GHz) [6]. The mean free path of 100 GHz vibrations versus temperature is shown in Fig. S3C. Our measured value is $\sim 10 - 20 \mu\text{m}$ from 30 K ($\sim 17.5 \pm 4 \mu\text{m}$) to 300 K ($\sim 10.5 \pm 2.2 \mu\text{m}$) with a weak temperature dependence.

II. RAW TRANSIENT GRATING DATA

Additional representative transient signals from TG are presented here. Shown are average heterodyne signals (10^4 averages) taken at a single location. Note that measured diffusivities in the main text were obtained by measuring multiple locations from which we determined the mean value and error bars.

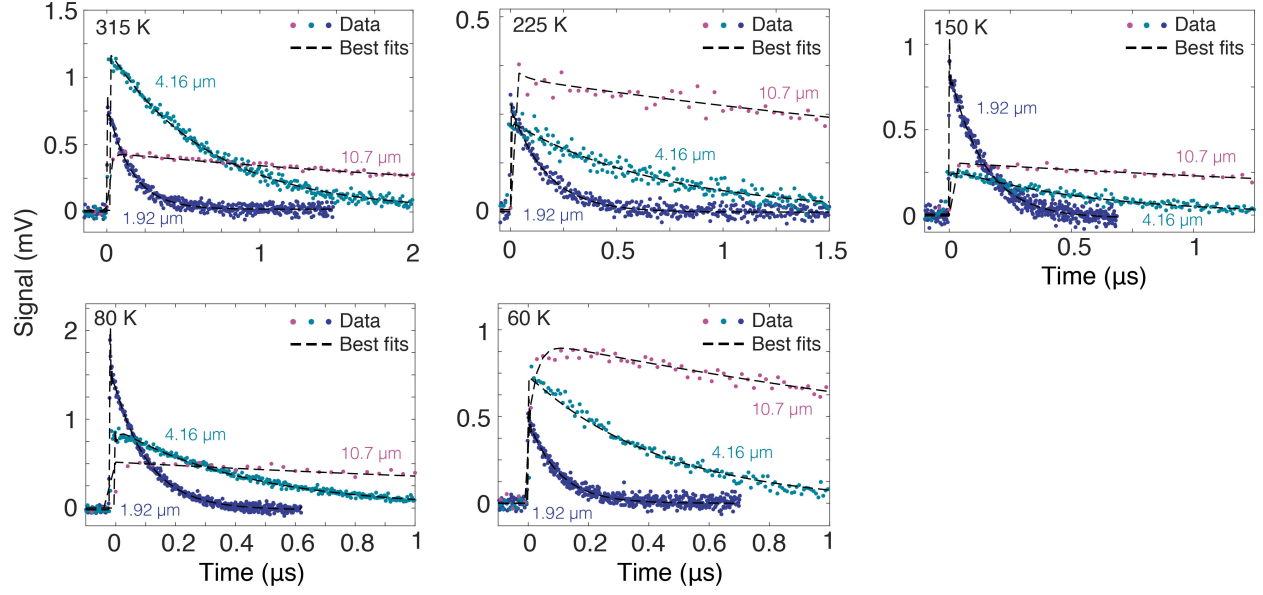


Figure S4. Measured TG signal versus time from 60 K to 315 K at several grating periods.

III. SELF-HEATING AND OPTICAL POWER

In this section, we present an estimation of the steady and transient temperature rises that occurred during the experiment and justify the chosen optical powers. Care was taken to minimize the steady state and transient temperature rise of the sample while maintaining a signal magnitude of at least 300 - 400 μV .

A. Temperature dependent optical properties in aSi

Estimating the self-heating requires knowledge of the optical absorptance of the sample. We measured temperature-dependent reflectance and transmittance from which we estimated the absorptance of the amorphous silicon film. Table SI shows the measured values. Accounting for optical reflections at various optical elements, the absorptance is around 50 - 55% at the temperatures in this study. For simplicity we use 60% for the calculations below.

Table SI. Optical properties of aSi measured at various temperatures.

Cryostat temperature (K)	Reflectance (%)	Transmittance (%)	Absorptance (%)
300	39	3	58
210	35	4	62
135	34	5	61
60	32	5	63
40	36	5	59

B. Steady heating

We estimate the steady heating due to the pump and probe pulses using a thermal resistor model in cylindrical coordinates. Consider the pump and probe beams as heat sources of radius $r_{pump} \equiv r_1$. The outer radius $r_2 \approx 500 \mu\text{m}$ of the membrane is fixed at the cryostat temperature. The cylindrical conduction resistance is $R = \ln(r_2/r_1)/(2\pi\kappa d)$ where κ is the bulk thermal conductivity of the membrane. The temperature rise is then

$$\Delta T = P_{abs,avg} \frac{\ln(r_2/r_1)}{2\pi\kappa d} \quad (\text{S2})$$

where $P_{abs,avg}$ is the absorbed average power of the laser beam. The absorbed average power was calculated using $P_{abs,avg} = \alpha P_{inc,avg} = \alpha P_{peak} D$ where $P_{inc,avg}$ is the incident average power on the sample, P_{peak} is the peak power incident on the sample and D is the duty cycle of the laser beam (1 for pump and 0.032 for probe from a chopper wheel).

Table SII shows the estimated steady temperature rise where T_h is the cryostat temperature, κ is the thermal conductivity used for calculation, $P_{pu,inc,avg}$ ($P_{pr,inc,avg}$) is the incident average power of the pump (probe) on the sample, ΔT_{pu} (ΔT_{pr}) is the steady temperature rise due to pump (probe), and ΔT_{total} is the estimated total steady temperature rise of the sample, and T_{calc} is the estimated temperature of the sample.

Table SII. Estimation of the steady heating of the sample.

T_h (K)	κ (Wm ⁻¹ K ⁻¹)	$P_{pu,inc,avg}$ (μW)	$P_{pr,inc,avg}$ (μW)	ΔT_{pu} (K)	ΔT_{pr} (K)	ΔT_{total} (K)	T_{calc} (K)
300	1.5	41	134	3.4	11.2	14.6	~ 315
210	1	27	88	3.4	11.0	14.4	~ 225
135	0.85	48	71	7.0	10.5	17.5	~ 150
60	0.7	48	61	8.5	10.9	19.4	~ 80
40	0.55	44	46	10.1	10.5	20.6	~ 60

C. Transient heating

We estimate the impulsive temperature rise induced by the absorbed optical energy. The temperature rise ΔT can be estimated from

$$\Delta T = \frac{E_{abs}}{C_v V} \quad (\text{S3})$$

where E_{abs} is absorbed laser energy, V is the volume of the sample illuminated by the beam, and C_v is the volumetric heat capacity [7]). The volume $V = \pi r^2 d$ where $d \approx 500$ nm is the estimated thickness of the film, and r is the $1/e^2$ beam radius (pump: $260 \mu m$, and probe: $235 \mu m$).

The absorbed laser energy was calculated using $E_{abs} = \alpha E_{inc}$ where α is the measured absorptivity and E_{inc} is the laser energy. The incident laser energy was obtained using $E_{pu,inc} = P_{pu,inc}/f$ for pump and $E_{pr,inc} = P_{pr,inc} t_{chop}$ for probe where $E_{pu,inc}$ ($E_{pr,inc}$) is the pump (probe) energy incident on the sample, $P_{pu,inc}$ ($P_{pr,inc}$) is the incident pump (peak probe) power, f is the repetition rate of the pump (200 Hz), and the t_{chop} is the time duration of the probe (160 μs).

Table SIII shows the estimated transient temperature rise where T_{st} is the estimated temperature accounting for the steady temperature rise, C_v is the heat capacity at $T = T_{st}$ in Ref. [7], ΔT_{pu} (ΔT_{pr}) is the transient temperature rise due to pump (probe), and ΔT_{total} is the overall transient temperature rise of the sample.

Table SIII. Estimation of the transient heating of the sample at several temperatures.

T_{st} (K)	C_v (Jcm ⁻³)	$E_{pu,inc}$ (μJ)	$E_{pr,inc}$ (μJ)	ΔT_{pu} (K)	ΔT_{pr} (K)	ΔT_{total} (K)
300	2.27	0.2	0.7	0.5	2.0	~ 3
210	2	0.1	0.4	0.4	1.5	~ 2
135	1.5	0.2	0.4	0.9	1.6	~ 3
60	0.73	0.2	0.3	1.9	2.9	~ 5
40	0.52	0.2	0.2	2.4	3.1	~ 6

IV. TEMPERATURE DEPENDENCE OF κ_{IR}

This section shows the temperature dependence of the thermal conductivity above the Ioffe-Regel crossover frequency (~ 10 THz for LA and ~ 5 THz for TA)[8]. Figure S5A shows κ_{IR} versus temperature for each profile along with the prediction from Allen-Feldman theory. The theoretical prediction was computed using the expression for mode diffusivity in Ref. [9] and the quantum-corrected specific heat. The temperature dependence of the measurements generally agrees with the theory although the theory slightly underestimates the actual values. Figure S5B shows κ_{IR} normalized to its room temperature value along with the normalized heat capacity. The κ_{IR} trend with temperature matches that of the heat capacity.

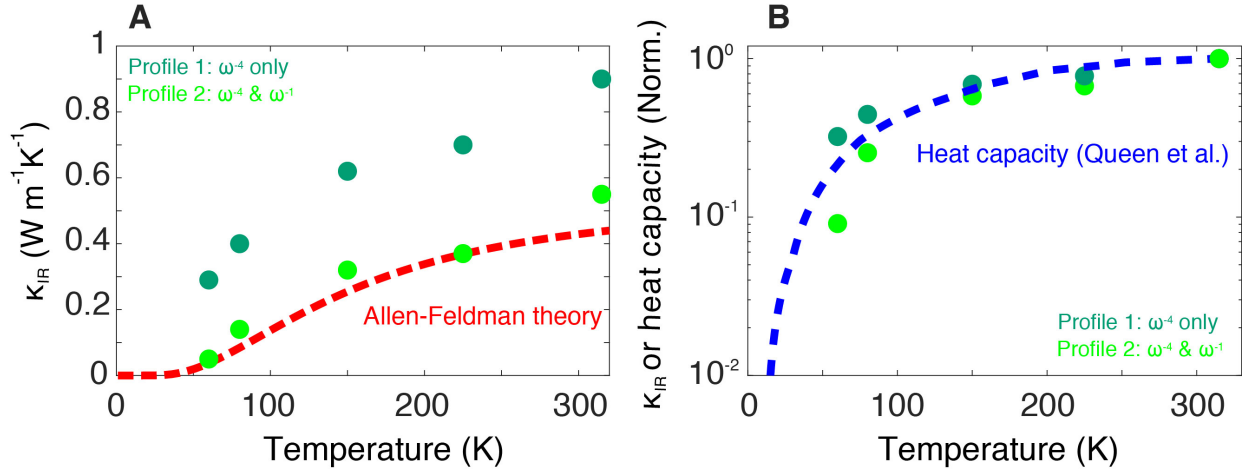


Figure S5. (A) Thermal conductivity (κ_{IR}) contributed by excitations above the IR frequency versus temperature for different MFP profiles discussed in the main text. The red dashed line is a prediction using harmonic approximation in disordered solid shown in Ref. [9, 10] for frequencies ≥ 10 THz for LA and ≥ 5 THz for TA. (B) The values in A normalized by their 315 K values along with the normalized heat capacity versus temperature (dashed blue line, Ref. [7]). The thermal conductivity (κ_{IR}) follows the temperature dependence of the heat capacity.

V. CROSSOVER FREQUENCIES AND κ_{IR}

This section presents additional information regarding the values of the crossover frequencies and κ_{IR} that are compatible with the data. The calculated relative differences between experiment κ_{expt} and the calculation κ_{calc} at 60 K using different κ_{IR} values $\kappa_{IR} = 0 - 0.2 \text{ Wm}^{-1}\text{K}^{-1}$ are shown in the left of Fig. S6. Blue regions in the left of Fig. S6 A - E indicate the cutoff frequencies that minimize the relative difference. We find that the optimized frequencies are in the range of 2-3 THz for LA and 1-2 THz for TA for all cases. As shown in the center column of Fig. S6 A - E, κ_{calc} at 60 K agrees with κ_{expt} for $\kappa_{IR} \leq 0.2 \text{ Wm}^{-1}\text{K}^{-1}$ above which the trend of κ_{calc} starts to deviate from that of κ_{expt} . The right column of Fig. S6 shows optimized κ_{IR} for 80 - 315 K using the optimized frequencies. The cutoff frequencies in the main text were selected to yield the overall best fit of thermal conductivity versus grating period at all temperatures. Therefore, although different choices for cutoff frequency and κ_{IR} are possible, the frequency-dependence of the MFPs remains unchanged. A steep slope ($n = 4$) in the sub-THz frequencies is necessary to explain the observed grating dependence of thermal conductivity.

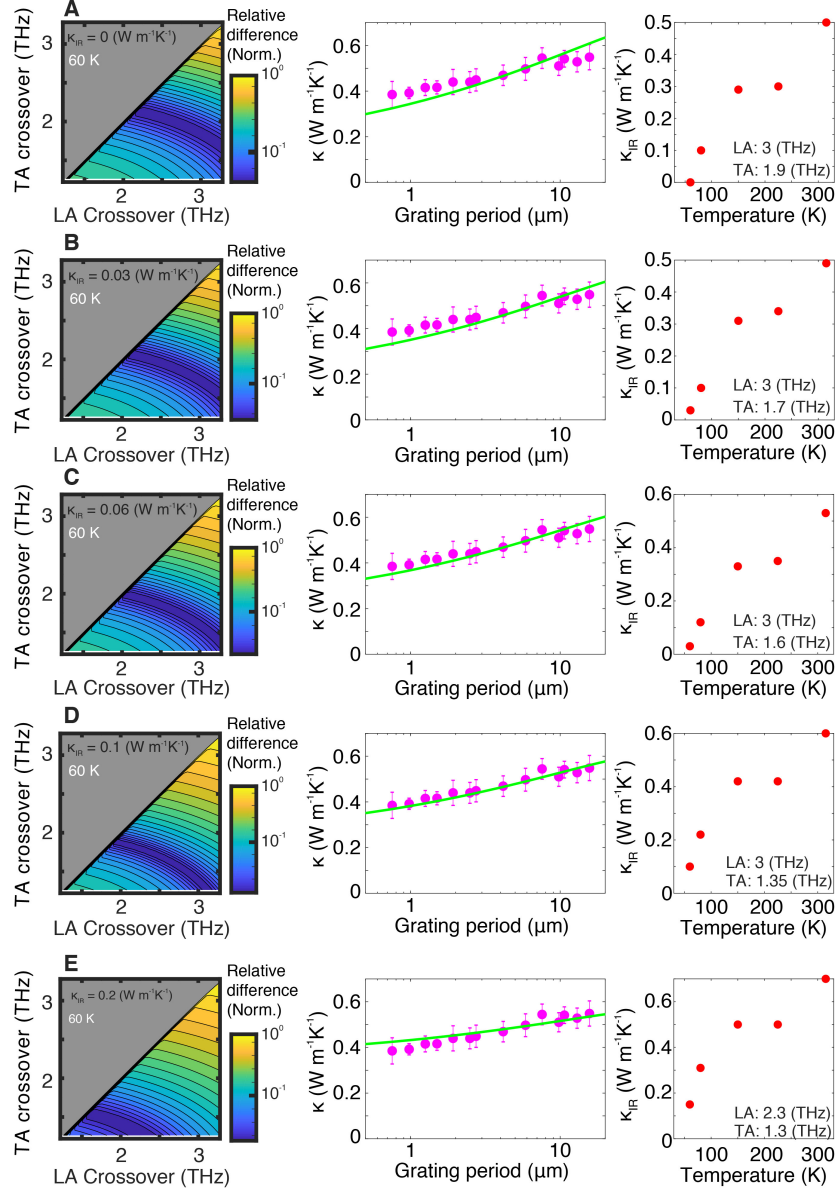


Figure S6. (Left) Calculated relative differences at 60 K for (A) $\kappa_{IR} = 0 \text{ W m}^{-1} \text{ K}^{-1}$, (B) $\kappa_{IR} = 0.03 \text{ W m}^{-1} \text{ K}^{-1}$, (C) $\kappa_{IR} = 0.06 \text{ W m}^{-1} \text{ K}^{-1}$, (D) $\kappa_{IR} = 0.1 \text{ W m}^{-1} \text{ K}^{-1}$, (E) $\kappa_{IR} = 0.2 \text{ W m}^{-1} \text{ K}^{-1}$. The blue area indicates the range of optimized LA / TA crossover frequency which minimize the relative difference. (Center) Calculated thermal conductivity versus grating period (κ_{calc}) using optimized crossover frequencies and experiments at 60 K. As the κ_{IR} increases, the slope of the κ_{calc} becomes less steep. (Right) Optimized κ_{IR} at higher temperatures using optimized crossover frequency determined from minimum relative difference at 60 K.

-
- [1] Kwangu Kang, Yee Kan Koh, Catalin Chiritescu, Xuan Zheng, and David G. Cahill. Two-tint pump-probe measurements using a femtosecond laser oscillator and sharp-edged optical filters. *Review of Scientific Instruments*, 79(11):114901, 2008. doi:10.1063/1.3020759. URL <https://doi.org/10.1063/1.3020759>.
- [2] D. B. Hondongwa, B. C. Daly, T. B. Norris, B. Yan, J. Yang, and S. Guha. Ultrasonic attenuation in amorphous silicon at 50 and 100 ghz. *Phys. Rev. B*, 83:121303, Mar 2011. doi:10.1103/PhysRevB.83.121303. URL <https://link.aps.org/doi/10.1103/PhysRevB.83.121303>.
- [3] Walter G. Mayer and E. A. Hiedemann. Optical methods for the ultrasonic determination of the elastic constants of sapphire. *The Journal of the Acoustical Society of America*, 30(8):756–760, 1958. doi:10.1121/1.1909753. URL <https://doi.org/10.1121/1.1909753>.
- [4] B. C. Daly, K. Kang, Y. Wang, and David G. Cahill. Picosecond ultrasonic measurements of attenuation of longitudinal acoustic phonons in silicon. *Phys. Rev. B*, 80:174112, Nov 2009. doi:10.1103/PhysRevB.80.174112. URL <https://link.aps.org/doi/10.1103/PhysRevB.80.174112>.
- [5] C. J. Morath and H. J. Maris. Phonon attenuation in amorphous solids studied by picosecond ultrasonics. *Phys. Rev. B*, 54:203–213, Jul 1996. doi:10.1103/PhysRevB.54.203. URL <https://link.aps.org/doi/10.1103/PhysRevB.54.203>.
- [6] C. Klieber, E. Peronne, K. Katayama, J. Choi, M. Yamaguchi, T. Pezeril, and Keith A. Nelson. Narrow-band acoustic attenuation measurements in vitreous silica at frequencies between 20 and 400 ghz. *Applied Physics Letters*, 98(21):211908, 2011. doi:10.1063/1.3595275. URL <https://doi.org/10.1063/1.3595275>.
- [7] D. R. Queen, X. Liu, J. Karel, T. H. Metcalf, and F. Hellman. Excess specific heat in evaporated amorphous silicon. *Phys. Rev. Lett.*, 110:135901, Mar 2013. doi:10.1103/PhysRevLett.110.135901. URL <https://link.aps.org/doi/10.1103/PhysRevLett.110.135901>.
- [8] Jaeyun Moon, Benoit Latour, and Austin J. Minnich. Propagating elastic vibrations dominate thermal conduction in amorphous silicon. *Phys. Rev. B*, 97:024201, Jan 2018. doi:10.1103/PhysRevB.97.024201. URL <https://link.aps.org/doi/10.1103/PhysRevB.97.024201>.
- [9] Philip B. Allen and Joseph L. Feldman. Thermal conductivity of disordered harmonic solids. *Phys. Rev. B*, 48:12581–12588, Nov 1993. doi:10.1103/PhysRevB.48.12581. URL <https://link.aps.org/doi/10.1103/PhysRevB.48.12581>.
- [10] Joseph L. Feldman, Mark D. Kluge, Philip B. Allen, and Frederick Wooten. Thermal conductivity and localization in glasses: Numerical study of a model of amorphous silicon. *Phys. Rev. B*, 48:12589–12602, Nov 1993. doi:10.1103/PhysRevB.48.12589. URL <https://link.aps.org/doi/10.1103/PhysRevB.48.12589>.